Universitat de les Illes Balears

BACHELOR'S THESIS

A New Computationally Efficient Model for Binary Neutron Star Coalescences

Felip Antoni Ramis Vidal

Degree in Physics

Faculty of Science

Academic Year 2021-22

A New Computationally Efficient Model for Binary Neutron Star Coalescences

Felip Antoni Ramis Vidal

Bachelor's Thesis

Faculty of Science

University of the Balearic Islands

Academic Year 2021-22

Key words:

Gravitational Waves, Neutron Stars, Precession, Tidal Effects, Waveform Model.

Thesis Supervisor's Name: Marta Colleoni

Tutor's Name (if applicable): Marta Colleoni

Abstract

We present the new computationally efficient `IMRPhenomXP_NRTidalv2` frequency-domain phenomenological tidal model for gravitational-wave signals coming from precessing binary neutron star coalescences. The model is composed of the frequency-domain binary black hole baseline `IMRPhenomXP` of [1] with the addition of a new precession version that is more suitable for binary neutron star coalescences, and the `NRTidalv2` tidal extension of [2], which adds the description of matter effects. We provide a general theoretical introduction to gravitational waves and the concepts behind the model with emphasis on precession and matter effects and compare different treatments of precession through timing tests and match calculations.

Abstracte

Presentem el nou model fenomenològic computacionalment eficient nadiu del domini de freqüència `IMRPhenomXP_NRTidalv2` per a ones gravitacionals procedents de coalescències de sistemes binaris d'estrelles de neutrons en precessió. El model està compost de la base nativa del domini de freqüència `IMRPhenomXP` [1] per sistemes binaris de forats negres, en la qual s'ha afegit una nova versió de precessió més adequada pels sistemes binaris d'estrelles de neutrons, i de l'extensió `NRTidalv2` [2] que incorpora els efectes provocats per la matèria. Oferim una introducció teòrica a les ones gravitacionals i els conceptes involucrats en la construcció del model amb èmfasi en els efectes de la precessió i la matèria. També comparem diferents tractaments de precessió mitjançant proves de cronometratge i de coincidència entre models.

Abstracto

Presentamos el nuevo modelo fenomenológico computacionalmente eficiente nativo del dominio de frecuencia `IMRPhenomXP_NRTidalv2` para ondas gravitacionales procedentes de coalescencias de sistemas binarios de estrellas de neutrones en precesión. El modelo está compuesto de la base nativa del dominio de frecuencia `IMRPhenomXP` [1] para sistemas binarios de agujeros negros, en la que se ha añadido una nueva versión de precesión más adecuada para los sistemas binarios de estrellas de neutrones, y de la extensión `NRTidalv2` [2] que incorpora los efectos provocados por la materia. Ofrecemos una introducción teórica en las ondas gravitacionales y los conceptos involucrados en la construcción del modelo con énfasis en los efectos de la precesión y la materia. También comparamos distintos tratamientos de precesión mediante pruebas de cronometraje y de coincidencia entre modelos.

Contents

1 Introduction

Gravitational waves were predicted by Einstein's General Theory of Relativity in 1916. However, it was not until 1974 (20 years after Einstein's death) that astronomers Russell Hulse and Joseph Taylor found indirect evidence of these waves by finding the first binary neutron star pulsar (a candidate system for radiating gravitational waves) and confirmed that the stars were approaching each other at the pace predicted by general relativity if they were emitting gravitational waves [3]. Observations of the same kind were repeated on other binary neutron stars as they were being discovered, until on the 14 of September 2015 (almost a century after their theoretical prediction), the Laser Interferometer Gravitational-Wave Observatory (LIGO) announced the first direct detection of gravitational waves coming from the binary black hole merger GW150914 [3].

Since the first detection in 2015, many more gravitational waves have been detected by the LIGO-Virgo network during the three observation runs that have taken place until now. So far, gravitational waves coming from binary black hole (BBH) systems, binary neutron star (BNS) systems, and binary systems composed of a black hole and a neutron star (NSBH) have been detected [4–6]. These waves interact very weakly with matter and reach Earth fairly unperturbed, which makes them a precious channel for obtaining information from astronomical bodies, especially from those that would otherwise be invisible (or very difficult to detect) in the electromagnetic spectrum. For example, they provide a unique method of measuring the properties of black holes and neutron stars and may hold the key to revealing precious information about the states of matter in their cores [7].

A key component of gravitational-wave detection and parameter estimation of the source properties is the existence of good theoretical waveform models. The purpose of this thesis is to study the performance of a new computationally efficient frequency-domain phenomenological tidal model for precessing binary neutron star coalescences, `IMRPhenomXP_NRTidalv2`. In this introductory section, we will explain some general concepts regarding gravitational waves, gravitational-wave sources, and gravitational-wave data analysis; in section 2 we will go into the details of precession and introduce a new precession version implemented in `IMRPhenomXP` for the construction of the tidal model; in section 3 we will explain matter effects and how are these modelled in `NRTidalv2`; and finally, in section 4 we will introduce the combination of those components into the new model `IMRPhenomXP_NRTidalv2` and present timing and match tests.

1.1 Gravitational Waves

The General Theory of Relativity (GR) states that gravity is a manifestation of the geometric properties of spacetime. In the theory, the presence of energy or momentum produces curvature in the four-dimensional spacetime, and matter travels along the geodesic lines (the generalization of straight lines on curved spaces) of this spacetime.

The fundamental object of the theory is the *metric tensor field*, $g_{\mu\nu}$, which contains information about the geometry of spacetime. This tensor field is determined by solving *Einstein's field*

equations,

$$G_{\mu\nu} + \Lambda g_{\mu\nu} = \frac{8\pi G}{c^4} T_{\mu\nu} \,, \tag{1}$$

where G is the *gravitational constant*, Λ is the *cosmological constant* (which has to do with the expansion of the universe), $T_{\mu\nu}$ is the *energy–momentum tensor* (which acts as the source), and

$$G_{\mu\nu} = R_{\mu\nu} - \frac{1}{2} R g_{\mu\nu} \tag{2}$$

is the *Einstein tensor*, which obeys the *Bianchi identity* $\nabla^\mu G_{\mu\nu} = 0$. The *Ricci tensor*, $R_{\mu\nu}$, and *Ricci scalar*, R, that appear on the definition of the Einstein tensor are constructed in terms of the *Christoffel symbols*,

$$\Gamma^\lambda_{\mu\nu} = \frac{1}{2} g^{\lambda\rho} \left(\partial_\mu g_{\nu\rho} + \partial_\nu g_{\mu\rho} - \partial_\rho g_{\mu\nu} \right) \,, \tag{3}$$

in the following way:

$$R = g^{\mu\nu} R_{\mu\nu} \,, \qquad R_{\mu\nu} = R^\sigma{}_{\mu\sigma\nu} = \partial_\sigma \Gamma^\sigma_{\mu\nu} - \partial_\nu \Gamma^\sigma_{\mu\sigma} + \Gamma^\lambda_{\mu\nu} \Gamma^\sigma_{\lambda\sigma} - \Gamma^\lambda_{\mu\sigma} \Gamma^\sigma_{\lambda\nu} \,. \tag{4}$$

In vacuum, the energy-momentum tensor is null and the equations simplify to $R_{\mu\nu} = \Lambda g_{\mu\nu}$. Furthermore, if we take $\Lambda = 0$, which implies ignoring those effects provoked by the expansion of the universe, the equations further simplify to $R_{\mu\nu} = 0$. The Einstein field equations are the fundamental tools modern physics employs to describe incredibly fascinating phenomena like black holes (BHs) and gravitational waves (GWs).

1.1.1 Gravitational Waves: Linearized Theory in Vacuum

Although very compact in tensor notation, Einstein's field equations are a system of ten coupled, non-linear, partial differential equations, whose general solution remains a formidable challenge [8]. However, when gravity is sufficiently weak, one can work in the regime of linearized gravity and consider small gravitational perturbations around a fixed background. Let us assume the background spacetime to be flat and choose a coordinate system x^μ in which the metric takes the form:

$$g_{\mu\nu} = \eta_{\mu\nu} + h_{\mu\nu} \,, \qquad |h_{\mu\nu}| \ll 1 \,, \tag{5}$$

where, in cartesian coordinates, $\eta_{\mu\nu} = \mathrm{diag}(-1, 1, 1, 1)$ is the Minkowski metric, and $h_{\mu\nu}$ are the small perturbations we are considering. Next, by introducing the above expression into the definition of the Ricci tensor and discarding all terms that are not linear in $h_{\mu\nu}$, one obtains that Einstein's equations (without the cosmological constant) can be written as:

$$\Box \bar{h}_{\mu\nu} + \eta_{\mu\nu} \partial^\rho \partial^\sigma \bar{h}_{\rho\sigma} - 2 \partial^\rho \partial_{(\mu} \bar{h}_{\nu)\rho} = -\frac{16\pi G}{c^4} T_{\mu\nu} \,, \qquad \bar{h}_{\mu\nu} = h_{\mu\nu} - \frac{1}{2} h \eta_{\mu\nu} \,, \qquad h = \eta^{\mu\nu} h_{\mu\nu} \,; \tag{6}$$

where $\Box = \eta^{\mu\nu} \partial_\mu \partial_\nu$ is the d'Alembertian operator in flat space, the parentheses mean the indices are symmetrized according to $2A_{(\mu\nu)} = A_{\mu\nu} + A_{\nu\mu}$ for any tensor $A_{\mu\nu}$, and we have defined the *trace-reversed* perturbation $\bar{h}_{\mu\nu}$ [9, 10].

As explained in the first paragraph, the coordinate system x^μ, must be chosen so that the restriction of small perturbations, $|h_{\mu\nu}| \ll 1$, holds. However, after such choice, one is left with

a residual gauge symmetry that can be exploited to further simplify eq. (6) [9]. The symmetry in question is the ability to perform transformations of coordinates of the form

$$x^\mu \;\rightarrow\; x^{\mu'} = x^\mu + \xi^\mu(x)\,, \tag{7}$$

upon which the perturbations transform as:

$$h_{\mu\nu} \;\rightarrow\; h'_{\mu\nu} = h_{\mu\nu} - 2\partial_{(\mu}\xi_{\nu)}\,, \qquad \bar{h}_{\mu\nu} \;\rightarrow\; \bar{h}'_{\mu\nu} = \bar{h}_{\mu\nu} - 2\partial_{(\mu}\xi_{\nu)} + \eta_{\mu\nu}\partial_\rho\xi^\rho\,; \tag{8}$$

where we must impose that $|\partial_\mu\xi_\nu|$ is at most comparable to $|h_{\mu\nu}|$ for the restriction of small perturbations to be preserved [9, 10]. The remaining freedom of choice for ξ^μ can be exploited to set the *Lorenz gauge*, $\partial^\nu\bar{h}'_{\mu\nu} = 0$, for imposing this restraint on eq. (8) provides $\Box\xi_\mu = \partial^\nu\bar{h}_{\mu\nu}$, which is always solvable [9]. This choice of gauge reduces eq. (6) to a wave equation, thus revealing why we talk about gravitational waves,

$$\Box\bar{h}_{\mu\nu} = -\frac{16\pi G}{c^4}T_{\mu\nu}\,. \tag{9}$$

Furthermore, there still is remaining gauge freedom within the Lorenz gauge, for it is preserved by transformations of the form $\xi_\mu \;\rightarrow\; \xi'_\mu = \xi_\mu + \zeta_\mu$, as long as $\Box\zeta_\mu = 0$, which is always invertible as well [9]. In vacuum, i.e. where $T_{\mu\nu} = 0$, these extra gauge freedom can be exploited to set[1] $\bar{h} = 0$ and $h^{0i} = 0$, which together with the fact that time-independent components are irrelevant for the GW, allows us to summarize our gauge choices into ([9]):

$$h^{0\mu} = 0\,, \qquad h^i{}_i = 0\,, \qquad \partial^j h_{ij} = 0\,. \tag{10}$$

This choice is known as the *transverse-traceless* gauge, in which the perturbation is usually denoted by h^{TT}_{ij}. Out of the 16 a priori independent components of a rank 2 tensor on a four-dimensional manifold, the perturbation $h_{\mu\nu}$ loses 6 due to the symmetry requirement of the metric, and each of our gauge choices further reduces it by 4, which leaves us with only 2 independent components. In this gauge $\bar{h}^{\mathrm{TT}}_{\mu\nu} = h^{\mathrm{TT}}_{\mu\nu}$, and the general solution to $\Box h^{\mathrm{TT}}_{\mu\nu} = 0$ can be written as

$$h^{\mathrm{TT}}_{ab}(t,z) = \begin{pmatrix} h_+ & h_\times \\ h_\times & -h_+ \end{pmatrix}_{ab} \cos\left[\omega(t - z/c)\right]\,, \tag{11}$$

where we have chosen z as the axis of propagation, $a, b \in \{1, 2\}$ are indices in the transverse (x, y) plane, and $h_+, h_\times$ are the amplitudes of the two independent polarizations of the wave [9]. The notation is related to the way in which different polarizations of gravitational waves would deform a ring of test particles in the plane transverse to their propagation.

1.1.2 Gravitational Waves in Curved Backgrounds

In curved backgrounds, it is not trivial to differentiate GWs from the background, though it is still possible if there is a separation of spacial or temporal scales allowing to distinguish between

[1] We are using the conventional index notation in which Greek indices go over all the coordinates (e.g. $\mu = 0, 1, 2, 3$) and Latin indices only over the three spacial coordinates (e.g. $i = 1, 2, 3$).

background and perturbations [10]. In this setting, the propagation equation of GWs in the Lorenz gauge, $\nabla^\mu \bar{h}_{\mu\nu} = 0$ (where ∇^μ is the dual of the covariant derivative), can be generalized to [11]

$$\Box \bar{h}_{\mu\nu} - R^{\lambda}{}_{\mu\nu}{}^{\sigma} \bar{h}_{\lambda\sigma} = 0 \,. \tag{12}$$

However, in order to find expressions for the energy and momentum carried by GWs, which is to say, in which way are GWs a source of spacetime curvature themselves, one must go beyond the linear theory over a Minkowski background [10]. Then, it is possible to obtain the GWs energy-momentum tensor by expanding Einstein's equations to second order[2] and taking averages of the physical quantities over a smaller time-scale than that of the background [10]. In the Lorenz gauge, the resulting expression is

$$T^{\mathrm{GW}}_{\mu\nu} = \frac{c^4}{32\pi G} \langle \nabla_\mu h_{\alpha\beta} \nabla_\nu h^{\alpha\beta} \rangle \ , \tag{13}$$

where the brackets denote the average [9, 10]. The energy density of the GWs can be obtained from the above expression, which in the TT gauge reads

$$\rho_{\mathrm{GW}} = T^{00}_{\mathrm{GW}} = \frac{c^2}{32\pi G} \langle \dot{h}_{ij} \dot{h}^{ij} \rangle \ , \tag{14}$$

where the dots stand for $\partial_t = c\partial_0$ [9, 10].

1.1.3 Gravitational Waves from Compact Binary Inspirals

In this subsection we will introduce some key concepts and equations regarding gravitational waves coming from binary systems of two compact stars, which are our sources of interest.

For weak-field sources, eq. (9) of the linearized theory over a flat background can be used. This equation can be solved analytically, and for non-relativistic sources (in which the velocities are much smaller than the speed of light), it provides, to lowest order in v/c, the *mass quadrupole formula* for GWs

$$h^{\mathrm{TT}}_{ij}(t, \vec{r}) = \frac{1}{r} \frac{2G}{c^4} \ddot{Q}^{\mathrm{TT}}_{ij}(t - r/c) \,, \tag{15}$$

where Q^{TT}_{ij} is the trace-free part of the mass quadrupole tensor of the source in the TT gauge, and $t - r/c$ is the *retarded time* (which accounts for propagation effects) [9]. This is to say, the GWs coming from a binary system (or any system for all that matters) can be obtained to lowest order by calculating the mass quadrupoles and applying the mass quadrupole formula.

In this quadrupole approximation, the total radiated power as GWs is given by

$$P_{\mathrm{quad}} = \frac{G}{5c^5} \langle \dddot{Q}_{ij} \ddot{Q}_{ij} \rangle \ , \tag{16}$$

where the brackets denote a temporal average over various GW periods, and the quadrupoles' derivatives must be evaluated at the retarded time [9]. For two point-mass particles in a circular

[2] It is needed to, at least, go to second order, for the oscillatory nature of the waves makes the averages of linear quantities disappear.

orbit, the above expression can be particularized to

$$P = \frac{32}{5}\frac{c^5}{G}\left(\frac{GM_c\omega_{\rm GW}}{2c^3}\right)^{10/3}, \tag{17}$$

where $M_c = [m_1^3 m_2^3/(m_1+m_2)]^{1/5}$ is the *chirp mass* and $\omega_{\rm GW}$ is twice the orbital angular frequency given by Kepler's law [9]. This expression shows how the emitted power grows with the angular frequency of the orbit, which in a binary coalescence increases as the bodies get closer, producing the characteristic "chirp" shape of the GWs in which the power reaches a maximum right before the bodies merge.

1.2 Properties of Gravitational-Wave Sources

Gravitational-wave sources can be widely grouped by the type of GW signals they produce. Following [3], these signals are broadly divided into *transient waveforms* and *continuous waveforms*. At the same time, transient waveforms are divided into *modelled transient waveforms* (for which we have good theoretical models) mainly produced by *compact binary coalescences*, and *unmodeled transient waveforms* (for which we do not have good theoretical models) mainly produced by *gravitational-wave bursts* coming from supernovae and neutron star quakes. Continuous sources are those that emit continuous gravitational-wave signals and can be divided into *narrow-band waveforms* which include GWs produced by spinning asymmetrical neutron stars, and *broad-band waveforms* which are identified with the *stochastic gravitational-wave background*.

To date, the vast majority of detected GWs have been transient waveforms coming from binary black hole (BBH) mergers [4–6, 12]. BBH mergers belong to the wider category of compact binary coalescences, which feature two compact objects (black holes or neutron stars) in a gradually shrinking orbit due to gravitational-wave radiation that eventually merge into a single object. In the case of BBHs, these can be modelled as Kerr (rotating) black holes until late in their evolution. A black hole binary in a quasi-circular orbit can be described generically by 15 parameters, some of which describe the relative position of the binary with respect to the detector (*extrinsic parameters*), whilst others encapsulate individual properties of the components (*intrinsic parameters*). By the *no-hair conjecture*, the intrinsic properties of Kerr black holes are uniquely determined only by their masses m_1 and m_2, and spins $\vec{S}_1$ and $\vec{S}_2$. These parameters are often re-expressed in terms of other variables, such as the mass ratio $q = m_2/m_1 \geq 1$, and dimensionless spins $\vec{\chi}_i = \vec{S}_i/m_i^2$ (in geometrized units) [13]. Other common mass parameters are: the *total mass* $M_T = m_1 + m_2$, *reduced mass* $\mu = m_1 m_2/M_T$, *symmetric mass ratio* $\eta = \mu/M_T$, and *chirp mass* $M_c = \eta^{3/5} M_T$.

Whilst the multipolar structure of the Kerr spacetime is entirely determined by the black hole's mass and spin, the multipole moments of a neutron star also depend on its internal structure.

[2]Since gravitational radiation tends to circularize binary system's orbits, this is typically a valid assumption for binaries formed in galactic fields, where the objects have time to shed their eccentricity by the time they enter into the LIGO band, and should hold until the bodies begin to combine or tidal effects become significant in the late stages of the inspiral [14]. On the other hand, binaries formed dynamically can still retain a non-negligible amount of eccentricity when they become observable [15]. Studies suggest the events observed until now come from both channels, making it necessary to model the effects of eccentricity [15].

Neutron stars can deform due to their intrinsic rotation or the gravitational field created by their companion [16]. These deformations are characterized by the *love numbers* that appear on the multipolar expansion of the star's gravitational field, which depend on the internal structure of the star, that is, on their *equation of state* (EoS). This way, continuous gravitational waves coming from rotating NS or transient waveforms coming from BNS coalescences can provide information on the EoS of neutron stars by putting constraints on the love numbers [16–18].

1.3 Binary Black Hole Baseline

In this section, we will describe the characteristics of gravitational-wave signals coming from binary black hole systems at each point in their evolution. These waveforms constitute the base on top of which matter effects can be included.

The life cycle of these systems can be split into three distinct stages [19]. The first and longest stage, the *inspiral*, is characterized by a separation between the objects much larger than their extents that diminishes at a rate that is much slower than the orbital frequency; the second stage, the *merger*, is characterized by a quick *plunge* when the objects reach their innermost stable circular orbital (ISCO), merging into a single object whilst emitting maximum GW power; and the last stage of the evolution, *post-merger*, consists in the relaxation of the resulting object until it becomes stationary[3] [13, 19].

If the spins are aligned (anti-)parallel to the orbital angular momentum (*aligned spin*), motion occurs in the fixed two-dimensional plane defined by $\vec{L}$, which is also the direction of maximum gravitational-wave energy emission [20]. However, in the general case where the spins have arbitrary orientations, relativistic spin-orbit and spin-spin effects originate precession of all angular momenta [12, 20]. In most configurations the system undergoes *simple precession*, where both spins and orbital angular momentum precess around the total angular momentum $\vec{J} = \vec{L} + \vec{S}_1 + \vec{S}_2$, which remains approximately fixed [20]. Less commonly, when $L \simeq S$ and $\hat{L} \sim -\hat{S}$, the system undergoes *transitional precession*, where $\vec{J}$ flips its direction [20].

In the case of aligned spin, the waveform presents monotonically increasing frequency and amplitude until the merger, where the amplitude reaches a maximum before quickly decaying during the ringdown, whilst the frequency keeps increasing until it slows down in the late ringdown (see fig. 1) [19]. In the general case, precession modulates the amplitude and phase of the aligned spin waveform, resulting in a substantially more sophisticated signal [12].

During the inspiral, binary black hole systems can be treated in the *post-Newtonian* (PN) approximation, which consists in systematically adding relativistic corrections to the Newtonian solutions in the expansion parameter[4] $\epsilon = v^2/c^2$. Approaching the merger, however, orbital velocities become comparable to the speed of light, and Einstein's field equations must be solved numerically. Nowadays numerical relativity simulations provide the waveforms emitted by BBHs thorough the merger and ringdown; however, GW data analysis applications require a continuous sampling across the parameter space, which makes of paramount importance the development

[3] In the case of binary black hole systems, the post-merger is referred to as *ringdown*, for the resulting object is another black hole that shows decaying gravitational perturbations until it becomes a stationary Kerr black hole.

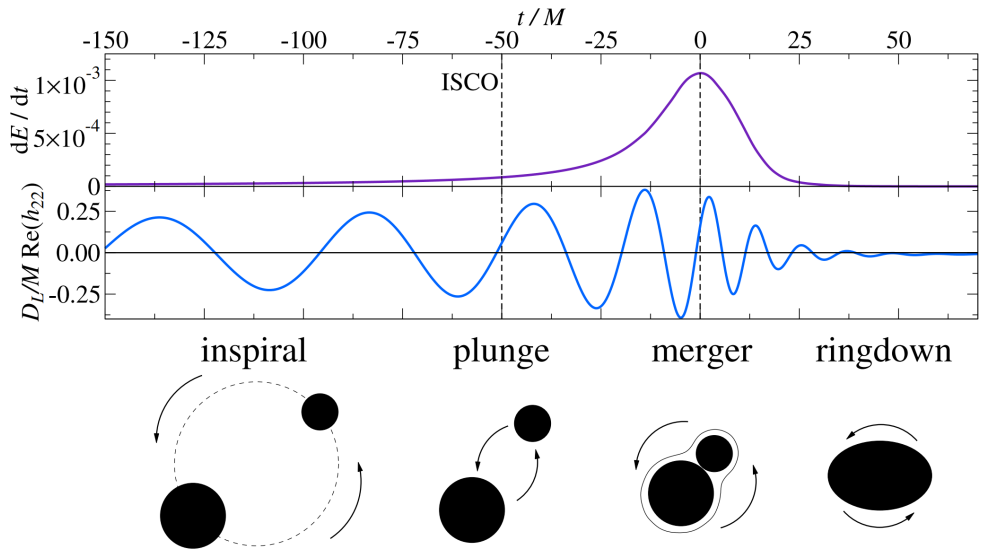

Figure 1: Evolution of the luminosity (top panel) and waveform (middle panel) emitted by a non-eccentric binary black hole system. Original from [19].

of semi-analytic models that provide a smooth connection between the post-Newtonian and numerical relativity solutions. Three types of waveforms are often used: *effective-one-body* (EOB) waveforms, *phenomenological* waveforms, and *numerical relativity surrogates* [13].

We focus on the frequency-domain (`X`) precessing (`P`) high-modes (`HM`) model `IMRPhenomXPHM` [1] from the `IMRPhenom` family of phenomenological waveforms, which provides piecewise (`IMR` stands for inspiral-merger-ringdown) closed-form expressions for the amplitude and phase of the GW signal that are fast to evaluate. In the `IMRPhenom` family, information coming from the PN approximation, perturbation theory and NR simulations is blended together to cover all the stages of coalescence [13].

1.4 Gravitational-Wave Data Analysis

LIGO detects gravitational waves using Michelson interferometers, where a laser beam is split and let travel along two arms before being reflected back and merged anew, producing an interference pattern. If arm lengths remain constant, the interference pattern will be static; if they do not, one can infer the change in length from the variation of the interference pattern [3].

However, gravitational waves reaching the Earth produce differences in length of thousands of times smaller than the diameter of a proton; this led to the development of a number of technological advancements in order to increase sensitivity and reduce noise [3]. The resulting enhanced interferometers are known as *power recycled Fabry-Perot Michelson interferometers* (details can be found in [3]).

Discerning gravitational wave signals from noise, that is, from any change of the interference pattern produced by something other than gravitational waves, is crucial for searches and systematic error prevention in parameter estimation [21]. Many forms of noise affect the data collected by LIGO, most of which is approximately stationary and therefore more easily treated in the fre-

[4]Solutions that are truncated at ϵ^n are said to be "expanded to the nth PN order", or simply "nPN".

quency domain [21]. Transient noise events (usually referred to as 'glitches') may mimic actual astrophysical signals in individual detectors but are rarely correlated between detectors [21].

In order to avoid as much of this noise as possible, LIGO has installed a series of noise prevention systems and deployed a series of sensors that collect data about the environment. The data collected by these sensors is used to generate noise models and detect environmental disturbances that might affect the interferometer [3].

In the long-wavelength approximation, where the wavelength of the gravitational wave is much longer than the size of the detector, one obtains that the interferometers have maximum sensitivity to waves propagating orthogonally to the arms plane and reduced sensitivity to other directions, with a few blind spots [3]. The existence of various gravitational wave detectors allows for all-sky coverage and validates simultaneous detections.

The data recorded by a detector d can be decomposed into noise n and gravitational wave signals $\mathfrak{h}$ as $d = h + n$. Generic transient searches look out for strong signals and allow for the discovery of new, unknown signals, but the existence of theoretical *signal models*, which we will denote with h, is critical to the detection of most, weak, signals [21].

When one has theoretical models for the expected signal, and the noise can be considered stationary and Gaussian, an optimal statistical detection method exists. This method is named *matched filtering*, and it consists in calculating the normalized *signal-to-noise ratio* (SNR) of the recorded data against a bank of model signals corresponding to different parameters of the source (usually referred to as *templates*) in search for values close to unity [21].

Stationary noise can be characterized, without loss of generality, by the following equations [9, 22] [5]

$$\langle n(t)\rangle = 0 \ , \qquad \langle \tilde{n}^*(f)\tilde{n}(f')\rangle \equiv \frac{1}{2} S_n(f)\delta(f-f') \ , \tag{18}$$

where $S_n(f)$ is named the *power spectral density* of the noise, which provides the average of the variance of the noise through

$$\langle n^2(t)\rangle = \int_0^\infty S_n(f) df \ . \tag{19}$$

One then defines the *filtered value* X of $x(t)$ as [23]

$$X = \int_{-\infty}^{\infty} x(t)F(t)dt = \int_{-\infty}^{\infty} \tilde{x}(f)\tilde{F}^*(f)df \ , \tag{20}$$

where $F(t) \in \mathbb{R}$ is the *filter function*, and uses this definition, together with eq. (18), to calculate the filtered value of the template in the presence of noise, S, and the root-mean-squared of the filtered value of the noise, N. The maximization of the signal-to-noise ratio (SNR) S/N yields the optimal expression of the filter function $\tilde{F}^*(f) \propto \tilde{h}(f)/S_n(f)$ ([9, 23]), named *optimal filter*, which is then used to define through eq. (20) the *noise-weighted inner product* between the signal and the template [22]

$$\langle d|h\rangle = 4\,\mathrm{Re}\int_0^\infty \frac{\tilde{d}(f)\tilde{h}^*(f)}{S_n(f)} df \ , \tag{21}$$

[5] From this point on, we are using $\tilde{x}$ to refer to the Fourier transform of x; and $\langle x\rangle$ to refer to the ensemble average of x over many repetitions, or, equivalently, to the time average in separate time intervals [9].

and the SNR as this inner product normalized with respect to the template [23]

$$\mathrm{SNR} = \frac{\langle d|h\rangle}{\sqrt{\langle h|h\rangle}} \ . \tag{22}$$

The previous result has been derived implicitly assuming that the signal is of the same duration as the template, whilst in reality, that will not be the case. We are interested in the matched filter as a function of the arrival time. This is achieved by writing $h(t) = p(t - t_0)$ where t_0 is the arrival time of the GW and $p(t)$ the theoretical waveform, which can be Fourier transformed into $\tilde{h}(f) = \tilde{p}(f)e^{-2\pi i f t_0}$, to give a complex time series [21, 22]

$$\langle d|h\rangle = 4\,\mathrm{Re}\int_0^\infty \frac{\tilde{d}(f)\tilde{p}^*(f)}{S_n(f)} e^{2\pi i f t_0} df \ . \tag{23}$$

The detection method consists then in looking for statistically significant peaks, by taking χ^2 tests into account, in the SNR time series whilst rejecting data containing noise glitches, which do not verify the assumptions of stationarity and Gaussianity and could lead to false detections [21]. Furthermore, a series of waveform consistency tests (which check the deviation of the data d from the model $n + h$) are implemented for those cases in which the sensors might not have picked up the glitch [21], and published results are required to have been detected with consistent parameters in at least two independent detectors [21].

Once a gravitational-wave detection is made, the next objective is to infer the physical parameters of its system of origin and their uncertainties. This procedure is done in the framework of Bayesian parameter estimation. If we denote by θ the parameters of our model $M(t;\theta) = n(t) + h(t;\theta)$, and I the background information, Bayes' theorem provides

$$p(\theta|d, M, I) = p(\theta|M, I)\frac{p(d|\theta, M, I)}{p(d|M, I)} \ , \tag{24}$$

where $p(\theta|d, M, I)$ is the *posterior probability density function* of the system having the parameters θ given that we have measured d with background information I; $p(\theta|M, I)$ is the *prior probability density function* (or *prior*) which contains our assumptions on how likely is to observe that combination of parameters; $p(d|\theta, M, I)$ is the *likelihood function* of observing d had the system had θ for parameters, which, assuming stationary Gaussian noise, takes the form

$$p(d|\theta) = \exp\left(-\frac{1}{2}\sum_i \left[(d_i - h_i(\theta)|d_i - h_i(\theta)) + \int \ln S_n^i(f) df\right]\right) \ , \tag{25}$$

where the sum is taken over the different detectors; and $p(d|M, I)$ is the *evidence*

$$p(d|M, I) = \int p(\theta|M, I)p(d|\theta, M, I)d\theta \ . \tag{26}$$

2 Modeling Precessing Binaries

Whenever the spins of a binary system are not aligned with the orbital angular momentum, all angular momenta undergo precession, significantly increasing the complexity of the dynamics and modulating the gravitational-wave signals [6]. Binary systems are expected to have spins with randomly distributed magnitudes and directions, making precession more usual than not [24]. This, together with the fact that having accurate waveform models is necessary for detection and crucial to parameter estimation, makes of fundamental importance the task of modelling precessing binaries.

Because precession involves all seven parameters (mass ratio and both vectorial spins), fully calibrating a model to NR is an incredibly challenging task, and some approximations have been introduced to reduce the dimensionality and complexity of the problem. One key aspect that can be leveraged for this purpose is the difference in the characteristic time scales of the orbital motion ($\tau_{\rm orb}$), precession ($\tau_{\rm prec}$), and radiation ($\tau_{\rm rad}$), for which we have $\tau_{\rm orb} \ll \tau_{\rm prec} \ll \tau_{\rm rad}$. This observation translates into precession having a subdominant effect on the GW phase during the inspiral and allows for a great simplification of the waveform by describing it in a *co-precessing frame* where the waveforms are characterized by the components of the spins parallel to the orbital angular momentum, which are approximately constant throughout the inspiral [20, 25]. The non-precessing waveforms in the (non-inertial) co-precessing frame can then be rotated into the (inertial) observer frame through a time-dependent rotation, obtaining precessing waveforms. This procedure is often referred as the "*twisting-up approximation*" in the literature [12, 20, 25].

In this section, we will explain how the twisting-up approximation is constructed in the frequency domain and introduce the analytical approximations of the rotation angles previously implemented in `IMRPhenomXP`, together with the new numerical integration implemented for the construction of `IMRPhenomXP_NRTidalv2`, following a strategy similar to `IMRPhenomTPHM`.

2.1 Twisting-up approximation

In the twisting-up approximation, the orbital angular momentum $\vec{L}$ is taken as the axis of the co-precessing frame[7], in which the gravitational waves are approximated by aligned-spin waveforms, and then the precession effects taken into account by rotating the waveforms according to the movement of the co-precessing frame as seen from an inertial frame of reference [12].

Let us define the relevant frames of reference we will be employing. The co-precessing frame (or L-frame) will have the orbital angular momentum as the z axis, $\hat{z} = \hat{L}$, and the other two axes will be given by the vector connecting the two black holes, such that $\vec{r} = r\hat{x}$ with $\vec{r} = \vec{r}_1 - \vec{r}_2$, and the right-hand rule $\hat{y} = \hat{z} \times \hat{x}$. Following up, let us define three relevant inertial frames of reference [1]. Because $\vec{L}$ precesses around $\vec{J}$, which is approximately fixed, it is a good choice to take $\vec{J}$ as the axis of an inertial frame[8], for the waveform modes will show a simple morphology in it; we will refer to such frame as the J-frame. In numerical relativity simulations, it is common

[6] Fortunately, precession does one good thing for us; it might help break degeneracies in parameter estimation.

[7] We will use the *Newtonian orbital angular momentum* $\vec{L}_{\rm N}$, which does not take into account the in-plane spins and points in the direction of the instantaneous angular frequency vector as a proxy for the actual orbital angular momentum $\vec{L}$, assuming the difference between the two is negligible [25].

to choose the initial spin components in the L-frame, which motivates us to define the L_0-frame as the L-frame evaluated at a certain reference time; this frame is commonly referred to as the *source-frame* [1]. The last frame we will introduce is that in which the z axis is given by direction towards the observer $\hat{N}$; this frame is most relevant for observational purposes, and we will refer to it as N-frame or *wave frame* [1].

In order to execute the rotation, the waveform is decomposed in the J-frame into a basis of -2 spin-weighted spherical harmonics

$$h^J(t;\boldsymbol{\lambda},\theta,\phi) = \sum_{\ell\geq 2}\sum_{m=-\ell}^{\ell} h^J_{\ell m}(t;\boldsymbol{\lambda})\,{}_{-2}Y_{\ell m}\,(\theta,\phi)\ , \tag{27}$$

where the intrinsic parameters $\boldsymbol{\lambda} = \{q, \vec{\chi}_1, \vec{\chi}_2\}$ are disentangled from the extrinsic orientation parameters (θ,ϕ) [25]. These modes are related to those in the L-frame by

$$h^J_{\ell m}(t) = \sum_{m'=-\ell}^{\ell} \mathcal{D}^{\ell *}_{mm'}(\alpha,\beta,\gamma) h^L_{\ell m'}(t)\ , \tag{28}$$

where (α,β,γ) are the Euler angles that provide the rotation from the J-frame to the L-frame, and $\mathcal{D}^{\ell *}_{mm'}$ are the complex conjugate of the Wigner D-matrices (further details in [26]). The angles α and β track the movement of $\hat{L}$, whilst γ is set by the condition of minimal rotation

$$\alpha = \arctan\left(L_y/L_x\right), \qquad \beta = \arccos\left(L_z\right), \qquad \dot{\gamma} = -\dot{\alpha}\cos\beta\ . \tag{29a-c}$$

As explained at the start of the chapter, the modes in the co-precessing frame are approximated by aligned spin ("AS") modes, that is

$$h^L_{\ell m}(t;q,\vec{\chi}_1,\vec{\chi}_2) \approx h^{\rm AS}_{\ell m}(t;q,\chi_{1\parallel},\chi_{2\parallel})\ , \tag{30}$$

where $\chi_{i\parallel}$ are the components of the dimensionless spins in the direction of the orbital angular momentum [25]. However, the aligned-spin modes must have their ringdown modified in order to take into account the final spin of the precessing system, which differs in general from the non-precessing case [25].

These modes can then be rotated into the wave frame (N-frame) through a time-independent rotation, and the GW polarizations (which are the measurable quantities at the detectors) constructed from

$$h(t) = h_+(t) - ih_\times(t)\ . \tag{31}$$

In order to work in the frequency domain, the time-domain expressions need to be Fourier transformed. Analytical closed-form expressions for such Fourier transforms can be obtained by applying the *stationary phase approximation* (SPA), which is valid throughout the inspiral [1].

[8] Taking $\vec{J}$ as fixed rules out the possibility of modelling systems that undergo transitional precession.

2.2 Euler angles throughout the inspiral

The Euler angles can be calculated by either numerically evolving the spin precession equations or by using analytical approximations such as the multiple scale analysis (MSA) [24]. We will test the accuracy and performance of these options at the end of the chapter. This subsection will introduce the specific equations for each approach to calculating the Euler angles.

2.2.1 Analytical approximations: effective single-spin and double-spin MSA

The *effective single-spin* description removes one black hole from the equations by modifying the spin components of the heaviest black hole into effective spin parameters that reproduce the original problem to a good approximation [20]. The two spin components parallel to $\vec{L}$, $\vec{S}_1^{\parallel}$ and $\vec{S}_2^{\parallel}$, are combined into an *effective spin parameter* $\chi_{\rm eff}$, and the four in-plane spin components $\vec{S}_1^{\perp}$ and $\vec{S}_2^{\perp}$ into an *effective precession spin parameter* χ_p with expressions:

$$\chi_{\rm eff} = \frac{m_1\chi_{1\parallel} + m_2\chi_{2\parallel}}{m_1+m_2} \qquad \text{and} \qquad \chi_p = \frac{1}{A_1 m_1^2}\max(A_1 S_1^{\perp}, A_2 S_2^{\perp})\,, \tag{32}$$

where $A_1 = (2+2/3q)$ and $A_2 = (2+3q/2)$ [20, 25]. If radiation reaction (the effects on the source due to the emission of GWs) is neglected, the evolution equations of the Euler angles in this single-spin case can be expressed in terms of the components of the total angular momentum $\vec{J} = \vec{L} + \vec{S}_1$ in the $\vec{L}$-frame (defined in section 2.1) as

$$\frac{d\alpha}{dt} = -\frac{\varpi J_x}{\sqrt{J_x^2+J_y^2}}\csc\beta\,, \qquad \frac{d\beta}{dt} = \frac{\varpi J_y}{\sqrt{J_x^2+J_y^2}}\,, \tag{33}$$

where ϖ is the *precession angular frequency* [27]. These expressions can be analytically solved to next-to-next-to-leading order in the spin-orbit coupling, and then γ be obtained by analytically solving eq. (29c) [25].

The MSA (*multiple scale analysis*) double-spin description exploits the difference in the characteristic time scales explained at the beginning of the chapter to introduce radiation reaction as a perturbation of the closed-form expressions of the conservative case [24]. The precession angles are expressed as a PN series with an extra MSA correction in terms of the orbital velocity or GW frequency; in the case of α, the solution can be split into two contributions:

$$\alpha = \alpha_{-1} + \alpha_0\,, \tag{34}$$

where α_{-1} is the leading-order term, and α_0 is the first correction that includes double-spin information [25]. A similar approach is taken for the γ angle, and the expression for the β angle, which defines the precession cone, is given by

$$\cos\beta = \hat{J}\cdot\hat{L} = \frac{J^2+L^2-S^2}{2JL}\,. \tag{35}$$

It is noteworthy that the MSA approximation assumes that the two bodies are black holes, which might introduce some errors when applying the model to binary neutron star coalescences. This is one of the reasons behind the introduction of the next precession version.

2.2.2 Numerical evolution of the spin precession equations

For the construction of `IMRPhenomXP_NRTidalv2`, the numerical evolution of the spin-precession equations has been implemented in the black-hole baseline `IMRPhenomXPHM`. This approach has the advantage of not introducing further approximations other than the SPA, which might be relevant for binaries involving neutron stars, for it means the coefficients of the spin-induced quadrupole moments are not necessarily set to those of a black hole.

Assuming conservation of the total angular momentum, $\dot{\vec{J}}(t) = \dot{\vec{L}}(t) + \dot{\vec{S}}_1(t) + \dot{\vec{S}}_2(t) \simeq 0$, the equations that provide the evolution of the precessing spins and orbital angular momentum are:

$$\frac{d\hat{L}}{dt} = \vec{\Omega}_{\hat{L}} \times \hat{L}\,, \qquad \frac{d\vec{S}_1}{dt} = \vec{\Omega}_1 \times \vec{S}_1\,, \qquad \frac{d\vec{S}_2}{dt} = \vec{\Omega}_2 \times \vec{S}_2\,, \tag{36a-c}$$

where Ω_L, Ω_1 and Ω_2 are *precession frequencies* that can be obtained in the Post-Newtonian theory to a given order in ϵ as functions of the binary's intrinsic parameters and of $v(t) = (\omega M_T)^{1/3}$, with ω being the derivative of the orbital phase [28]. Radiation reaction can be taken into account by letting the parameter evolve in time, according to

$$\dot{v} = -\frac{\mathcal{F}}{[dE/dv]}\,, \tag{37}$$

where $\mathcal{F}$ is the GW flux and E the binding energy of the binary [28].

These equations are solved by using the `SpinTaylor` infrastructure of the `LALSimulation` module in the `LALSuite` algorithm library, reason for which we will refer to this approach as the *SpinTaylor* version of the precession. Additionally, models belonging to the `IMRPhenomX` family adopt by default the *multibanding* (MB) algorithm, which evaluates the waveform on a grid that is adapted to the signal's morphology, finer in the inspiral, where the phase evolves more rapidly, and coarser in the ringdown, where it is sufficient to interpolate from a coarser grid [29].

Once $\vec{L}$ has been obtained by solving the spin precession equations (36a-c), it can be introduced in equations (29a-c) to obtain the Euler angles [25].

3 Tidal Effects and Their Imprints on GW Signals

The consideration of objects with matter distributions, such as neutron stars, adds an extra layer of complexity to the modelling of GWs.Namely, Einstein's field equations must be solved together with the equations of general relativistic hydrodynamics (which provide the kinematics of the matter distribution) [30]. However, there is much to gain from overcoming such complexity, for these systems represent unique sources of information about exotic states of matter at supra-nuclear densities, and GWs are the best carriers of such information [30].

To date, two BNS and several NSBH candidates have been detected by the LIGO Scientific Collaboration (LSC), and more are expected to be detected in the near future thanks to the increasing sensitivity of the detectors [6, 30]. However, the extraction of the source parameters of these systems depends crucially on the existence of accurate GW models for their emitted

signals, which are quite different from those of BBH systems.

In this section, we will introduce the fundamental effects of NSs' matter in GW signals, the basic concepts behind their modelling, and the most relevant models available to represent signals from BNS coalescences, with emphasis on `NRTidalv2`.

3.1 Tidal Effects in BNS Coalescences

The dominant tidal effects in BNS coalescences arise from the response of NSs to the spacetime bending produced by their companion [30]. The quasi-periodic orbit of a NS around its companion during the inspiral produces a time-varying tidal field that stimulates the NS's characteristic oscillation modes, which are determined by the properties of matter in its interior [30]. These oscillations produce a change in the structure of the external spacetime of the NS that grows more prominent the closer the stars get (see fig. 2). In the adiabatic regime, the effects of a star's internal structure can be characterized through the *tidal deformability parameters*, whose measure can provide insight on the EoS of the NS [30]. These effects leave imprints on the emitted GWs that accumulate over time (see fig. 3).

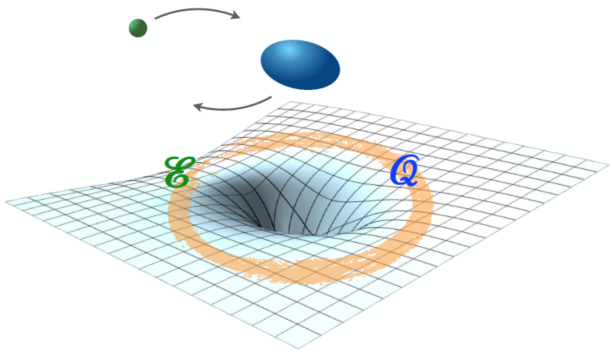

Figure 2: Drawing that illustrates the tidal deformation of the NS (blue) produced by the tidal field $\mathcal{E}$ of its companion (green). The change in the multipole structure of the NS's external spacetime $\mathcal{Q}$ will affect the emitted GWs. Picture obtained from [30].

Another matter effect arises in spinning NSs due to the deviations from spherical shape that rotation produces in the matter distribution and the coupling of this rotation with the tidal field of the companion star [30]. This translates into the appearance of *spin-induced multipole moments* in the multipolar decomposition of the NS's exterior spacetime that also depend on the EoS through the *rotational Love numbers* [30]. These spin-induced effects are at least quadratic in spin and enter at second PN order, whilst the tidal effects of the previous paragraph first enter at fifth PN order; this makes spin-spin effects dominant at lower frequencies and tidal effects dominant at higher frequencies [30]. All BNS systems to date have shown neutron stars with small dimensionless spin parameters, making the tidal contribution of higher relevance for these systems [2]. Nevertheless, it is still important to model spin effects, for there could be BNS systems with higher spins waiting to be discovered.

The post-merger is also greatly affected by matter effects; it involves complicated thermal and magnetohydrodynamical effects that make it much harder to model than the inspiral. In contrast

to BBH coalescences, where the resulting object is always a BH, BNS coalescences can produce a variety of outcomes depending on the initial masses and spins. These outcomes are qualitatively classified based on the total mass as: *prompt collapse*, *hypermassive*, *supramassive neutron stars* (SMNS) and *massive neutron stars* (MNS) [30]. If the total mass is higher than a certain threshold, the system undergoes prompt collapse into a BH, which might be surrounded by a low mass accretion disk [30]; if it is smaller than the threshold, the resulting object will be a neutron star surrounded by a more massive accretion disk. Depending on its baryonic mass, the remnant is classified into HMNS, SMNS or MNS (see Fig. 5 of [30]).

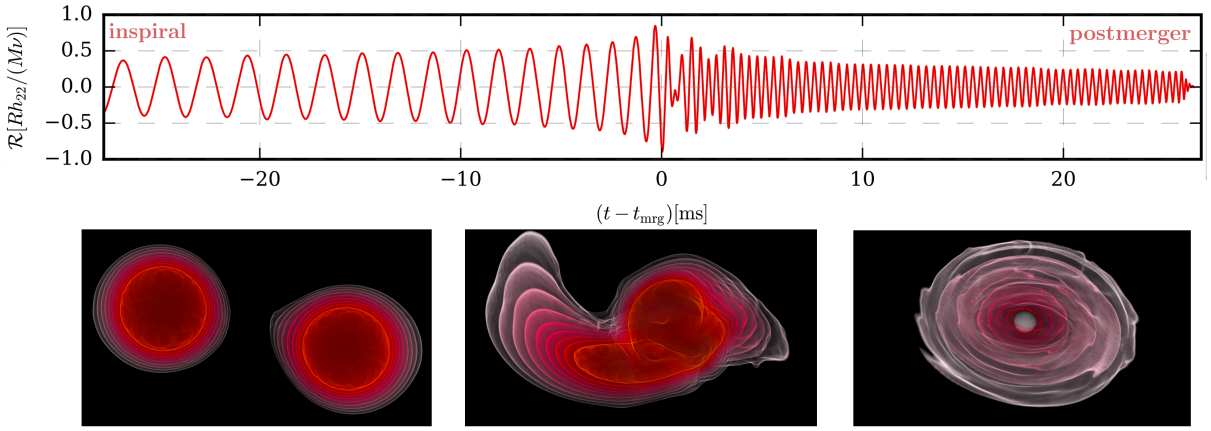

Figure 3: Numerical relativity simulation of a BNS system near merger. The top panel shows the emitted GW, and the bottom panel the rest-mass density evolution of the system, which develops into a BH with an accretion disk. Figure from [30].

3.2 Gravitational Field of Deformed Stars

We will now provide some mathematical insight on the concepts of the previous subsection by giving a Newtonian introduction that carries over to GR with the appropriate modifications of how the deformation of stars due to the gravitational field of their companion or their intrinsic rotation affects their gravitational potential.

Let us start with tidal deformations by considering a non-rotating NS with its center of mass as the origin of our non-inertial reference frame, together with an orbiting companion. In this setting the companion generates a gravitational field that produces a time-dependent perturbation $\delta\rho(t,\vec{r})$ to the spherical equilibrium configuration $\bar{\rho}(r)$ of the NS, such that its mass distribution can be written as $\rho(t,\vec{r}) = \bar{\rho}(r) + \delta\rho(t,\vec{r})$ [31]. This gravitational field can be expressed by means of a potential $U_{\rm ext}$, that verifies $\nabla^2 U_{\rm ext} = 0$ outside its source, and which can be Taylor expanded around the center of mass of the NS. The way in which the fluid dynamics equations that govern $\rho(t,\vec{r})$ depend on this potential (see [32] for details) makes irrelevant the constant and linear terms of such expansion and leads us to define the *tidal potential*

$$U_{\rm tidal}(t,\vec{r}) = -\sum_{\ell=2}^{\infty} \frac{1}{\ell!}\mathcal{E}_L x^L \,, \tag{38}$$

where $L = (a_1 \cdots a_\ell)$ is a *multi-index* with the property $x^L = x^{a_1}\cdots x^{a_\ell}$, and we are using the

Einstein summation convention [30, 32]. The quantities

$$\mathcal{E}_L = -\partial_L U_{\rm ext}(t, \vec{0}) \,, \tag{39}$$

where $\partial_L = \partial_{a^1} \cdots \partial_{a^\ell}$, are the *tidal moments* of the NS, which, since the contraction of any two of its indices produces a Laplacian, are symmetric and trace-free (STF) in all pairs of indices [30, 32]. As we will see, these are the relevant quantities regarding the NS's tidal deformation.

The gravitational potential generated by the deformed NS can be written as

$$U(t, \vec{x}) = G \int_{\mathbb{R}^3} \frac{\rho(t, \vec{r}\,')}{|\vec{r} - \vec{r}\,'|} d^3x' \,. \tag{40}$$

This expression can be expanded in multipoles outside the NS by performing the following Taylor expansion in $\vec{r}\,'$ of $|\vec{r} - \vec{r}\,'|^{-1}$ around the origin (center of mass),

$$\frac{1}{|\vec{r} - \vec{r}\,'|} = \frac{1}{r} + \sum_{\ell=1}^{\infty} \frac{(2\ell-1)!!}{\ell!} \frac{x^{\langle L\rangle}}{r^{2\ell+1}} x'^L \,, \tag{41}$$

where the brackets around the indices denote the STF projection of a tensor as in $x^{\langle ij\rangle} = x^i x^j - |\vec{x}|^2 \, \delta^{ij}$ (the general expression can be found in [32]), and which holds for $r > r'$ [30–32]. Upon the introduction of this expansion in eq. (40), the distribution of the integrals gives rise to the *Newtonian mass multipole moments*,

$$Q_L = \int_{\mathbb{R}^3} \rho(t, \vec{r}\,') x'^L d^3x' \,, \tag{42}$$

of which: the monopole is the mass of the NS, $M = \int \rho(t, \vec{r}\,') d^3x'$, and the dipole is zero when working in centre-of-mass coordinates [31]. With the above definition and the aforementioned remarks, the star's gravitational potential can be written as

$$U(t, \vec{x}) = \frac{GM}{r} + G \sum_{\ell=2}^{\infty} \frac{(2\ell-1)!!}{\ell!} \frac{Q_{\langle L\rangle} x^{\langle L\rangle}}{r^{2\ell+1}} \,, \tag{43}$$

where the reason behind taking the STF part of the multipole moments is that these appear contracted with $x^{\langle L\rangle}$, and the following is true for any two tensors A^L and B^L: $A^L B_{\langle L\rangle} = A^{\langle L\rangle} B_{\langle L\rangle}$ [32].

In the adiabatic limit, where the internal time scales of the NS are fast compared to the variations in the tidal field, the fluid equations show that the trace-free induced multipoles $Q_{\langle L\rangle}$ are proportional to the tidal STF moments $\mathcal{E}_L$,

$$Q_{\langle L\rangle} = -\lambda_\ell \, \mathcal{E}_L \,, \tag{44}$$

where λ_ℓ are the *tidal deformability parameters* that encapsulate the composition of the NS [30, 32]. Thus, deviation of the gravitational potential outside the star from that of a point mass only depends on the tidal moments and tidal deformability parameters. In order to simplify the form of eq. (43), these parameters are often re-expressed in terms of the dimensionless *tidal Love*

numbers k_ℓ, defined through

$$G\lambda_\ell = \frac{2}{(2\ell-1)!!} k_\ell R^{2\ell+1} \,, \tag{45}$$

where R is the radius of the unperturbed NS [30, 31].

The total gravitational potential outside the NS can be obtained by adding the external contribution of eq. (38) to the expanded potential of the NS, eq. (43); which after introducing eq. (44) in terms of the Love numbers, reads

$$U_T(t,\vec{r}) = \frac{GM}{r} - \sum_{\ell=2}^{\infty} \frac{1}{\ell!} \mathcal{E}_L x^L \left[1 + 2k_\ell \left(\frac{R}{r}\right)^{2\ell+1}\right] . \tag{46}$$

If rotation is introduced and its effect considered to be independent of the tidal deformation, its consequence is the appearance of new *spin-induced multipole moments* on the expansion of the NS's potential [30]. For example, the spin-induced quadrupole is given by

$$Q_2^{\mathrm{S}} \approx -\kappa \chi^2 M^3 \,, \tag{47}$$

where $\chi = cS/(GM^2)$ is the dimensionless spin, and κ is the spin-induced quadrupole parameter. While $\kappa = 1$ for a BH, this parameter can assume a range of values for a NS [30].

In GR, tidal effects are computed on the framework of perturbation theory over the equilibrium configuration of the NS [31]. In this framework, the perturbations of the metric are separated into polar and axial modes, the coefficients of which define two families of Love numbers [31]. The Love numbers associated with the polar modes are called "electric-type" and those associated with axial modes, which disappear in the Newtonian limit, are called "magnetic-type" [31].

3.3 Tidal Waveform Models for BNS Coalescences

There are various approaches to modelling the tidal effects produced by matter distributions. In BNS coalescences, a significant fraction of the SNR is accumulated during the inspiral, and, therefore, a natural approach is that of working within the PN framework. However, as we discussed earlier, the PN approximation is doomed to break down near merger, and hence a waveform model describing the complete coalescence will need some input from NR. Other approaches have been developed to alleviate this problem: *tidal* EOB *models*, which combine PN theory results with strong-field effects in the test-particle limit by using the effective-one-body formalism, and *phenomenological tidal models*, which extend BBH approximants with a tidal description that includes finite-size effects of the NSs fitted to NR simulations, and which we will be considering in this text [30].

The basic assumption of the phenomenological approach is that the BNS waveform phase can be decomposed as a sum of a non-spinning point-particle (pp) contribution, a spin-orbit (SO) coupling contribution, a spin-spin (SS) contribution, a tidal (T) contribution that accounts for the deformation of the NS due to the gravitational field of its companion (see fig. 2), and higher

order spin-tidal coupling effects [2, 30]

$$\psi(f) = \psi_{\rm pp}(f) + \psi_{\rm SO}(f) + \psi_{\rm SS}(f) + \psi_{\rm T}(f) + \cdots \ .$$

The point-particle and spin-orbit contributions are unchanged with respect to their BBH counterparts, but the spin-spin contribution depends now on the star's internal structure through the rotational Love numbers that appear along the spin-induced multipole moments introduced in the previous subsection. The new tidal contribution does, of course, depend on internal structure through the Love numbers, as well [2, 30].

Because of the decrease in detector sensitivity at higher frequencies, the post-merger is expected to be negligible for current detectors[9], which is why nowadays phenomenological waveforms are smoothly tapered around the merger [33]. However, the smooth frequency and amplitude development even beyond the point of merger should prevent biases in parameter estimation. This, together with the fact that BNS inspirals present more cycles than those of BBH (because of the smaller masses), allows us to obtain relevant information from the inspiral alone [30, 34].

In this work, we focus on the `NRTidalv2` [2] approximant, which includes quadrupolar and octupolar spin-spin and cubic-in-spin effects up to 3.5PN order and provides closed-form approximations for the tidal contributions to both phase and amplitude that are fitted to numerical relativity simulations; furthermore, it can be added on top of any BBH baseline. In it, the taper is introduced by multiplying the total amplitude by a window function as

$$\tilde{A} = (\tilde{A}_{\rm BBH} + \tilde{A}_{\rm T}^{\rm NRTidalv2}) \times \tilde{A}_{\rm Planck} \ , \tag{48}$$

where $A_{\rm BBH}$ is the amplitude of the BBH baseline, $A_{\rm T}^{\rm NRTidalv2}$ is the tidal correction provided by `NRTidalv2`, $A_{\rm Planck}$ is the *Planck taper* introduced in [35], and the tildes indicate that these functions are in the frequency-domain.

4 Performance of the Model

After having introduced `IMRPhenomXP` and `NRTidalv2` in previous sections, we will now present the tests we have run in order to evaluate the performance of the combination of these approximants into `IMRPhenomXP_NRTidalv2`. Additionally, we will provide tests of the `SpinTaylor` version of the Euler angles implemented in `IMRPhenomXP` for the construction of the model.

4.1 Baseline Matches

In this subsection we will present matches against binary black-hole numerical relativity waveforms of the `MSA` and `SpinTaylor` precession versions of `IMRPhenomXP`. As we mentioned earlier, the binary black-hole model is the baseline on top of which matter effects are added: therefore, the matches below will give information about the performance of the model in the limit of zero tidal deformability.

[9] It is expected that next-generation instruments will have enough sensitivity for these effects to be relevant.

The *match* $\mathcal{M}$ between two waveforms is defined as the noise weighted inner product of eq. (21) normalized to unity[10] and maximized over the relative time and phase shifts between waveforms [1]. For a precessing system, one also needs to maximise over the polarization angle ψ_0 and the orientation of the in-plane spins at the reference frequency, α_0. That is, the match is defined as

$$\mathcal{M}(h_1, h_2) = \max_{t_0,\phi_0,\psi_0,\alpha_0} \frac{\langle h_1|h_2\rangle}{\|h_1\|\|h_2\|} \,, \tag{49}$$

where $\|h_i\| = \sqrt{\langle h_i|h_i\rangle}$; and we will refer to $1-\mathcal{M}$ as the *mismatch*. For the calculation of these matches, we have used the Advanced-LIGO design sensitivity power spectral density [36] with a lower cutoff at 20 Hz and an upper cutoff at 2048 Hz, exactly as in the original `IMRPhenomXPHM` paper [1]. We have also used the same set of 99 NR precessing SXS waveforms ([37]) employed in [1] over five total masses ranging from 50 to 250 solar masses, three inclinations (the angle between the line of sight and the orbital angular momentum at the reference frequency) between 0° and 90°, and five values for both the polarization angle of the source and signal phase at the reference frequency. The polarization angle and reference phase, denoted below by the index i, are "averaged over" in the SNR-*weighted match*,

$$\mathcal{M}_w = \left[\frac{\sum_i \mathcal{M}_i^3 \left\|h_i^{\rm NR}\right\|^3}{\sum_i \left\|h_i^{\rm NR}\right\|^3}\right]^{1/3} \,, \tag{50}$$

for each total mass and inclination, which reduces the relevance of those match values with a low probability of being detected [1].

Starting with an overview of the results, we can observe in the histogram of fig. 4 how both precession versions produce very similar mismatch distributions with the majority of values being in the 10^{-2} to 10^{-3} range. `SpinTaylor` does come somewhat on top of `MSA` by having a slightly smaller median and a $\sim 60\%$ of the standard deviation, which translates into better consistency and fewer mismatches on the high tail of the distribution. The results observed here are entirely consistent with what was previously observed for `IMRPhenomTPHM` [25], where the same precession prescription was implemented. More marked improvements might come after re-calibrating the aligned-spin baseline and incorporating calibration to NR for the Euler angles as done in [12].

When the results are broken down by inclination and total mass as in the box plots of fig. 5, both versions show larger median mismatches the greater the inclination but also smaller spreads with fewer mismatches above 10^{-1} than the face-on case. Comparing the versions, we observe a slight improvement in the `SpinTaylor` matches for $\iota = \pi/3$ rad and $\iota = \pi/2$ rad. On the other hand, for $\iota = 0$ rad (face-on sources), the median values of `SpinTaylor` are slightly higher than those of `MSA`, but the former shows less outliers.

In the line plots of fig. 6 we can see how `SpinTaylor` produces fewer mismatches above the fiducial value of 5%, and that when it does, `MSA` does as well with worse values. Furthermore, all of these happen for the `BBH:0062` and `BBH:0165` SXS waveforms, which correspond to strongly

[10] By using the Cauchy–Schwarz inequality for real inner products $\langle h_1, h_1\rangle \leq \|h_1\|\|h_2\|$.

precessing (high in-plane spins) high mass-ratio binaries, which display intricate interactions between various multipole modes [1].

4.2 Tidal Matches

In this subsection we will present match tests of `IMRPhenomXP` with the `NRTidalv2` extension. We will start by analyzing the aligned spin case and then move on to precession. We stress here that matter effects will enter in both the co-precessing frame signals and the Euler angles that twist those waveforms into precessing ones, but only the `SpinTaylor` precession version contains both.

In the aligned spin case, we compare several tidal models on a random sample of 5000 binaries drawn from a high-spin prior, where the spin magnitudes are required to satisfy $a_i \leq 0.89$ and the mass ratio is allowed to take values between 1 and 3. We expect to see increasing disagreement with other models for systems with non-negligible spins, as a number of spin-dependent effects (such as tides and quadratic-in-spin effects) are incorporated in different ways by different models. It should also be noted that the `NRTidalv2` extension was calibrated only to a small number of non-spinning equal-mass NR hybrids: therefore, we expect that some extrapolation will be present in other regions of parameter space.

The matches presented here compare our new model `IMRPhenomXAS_NRTidalv2` with its phenomenological predecessor `IMRPhenomD_NRTidalv2` as well as with two models of the EOB family, i.e. `TEOBResumS` [38] and `SEOBNRv4T` [39] over the same random set of parameters. We grouped our results into the histogram of fig. 7a and the scatter plots of fig. 8. In these plots, we observe an excellent agreement between the two `NRTidalv2` phenomenological models, with only a 0.3% of matches below 0.97 and a median mismatch of 0.0012. There is also a generally good agreement with `TEOBResumS`, whilst more differences can be seen with `SEOBNRv4T`, especially for high spin configurations. This might be related to the fact that `SEOBNRv4T` has a more complete description of tidal effects which includes dynamical tidal effects, whilst the current version of `TEOBResumS` does not, putting it closer to `NRTidalv2`. In conclusion, as expected, all three models agree quite well for low spin configurations, but discrepancies grow larger the higher the spin and mass ratio, which hints at issues with waveform systematics.

Regarding precession, and in the absence of sufficiently long precessing binary neutron star hybrids, we chose to compare precessing tidal models among them. In this case the matches have been run between the `SpinTaylor` and `MSA` versions of `IMRPhenomXP`, and against `IMRPhenomPv2`, both with the `NRTidalv2` tidal extension and over the same set of random, precessing, BNS systems, with spin magnitudes $a_i \leq 0.89$, spin tilts isotropically distributed and uniform priors on the component's masses $1\,M_\odot \leq m_1, m_2 \leq 3\,M_\odot$. As in the aligned case, we have grouped the results into a histogram (fig. 7b) and a scatter plot (fig. 9).

What we observe is that, when we add precession, the excellent agreement between Phenom models is lost. The results show 36.2% of matches below 0.97 and a median mismatch of 0.012 for `IMRPhenomXP(MSA)` against `IMRPhenomPv2`, and 41.3% of matches below 0.97 and a median mismatch of 0.019 for `IMRPhenomXP(SpinTaylor)` against `IMRPhenomPv2`; which are one order of

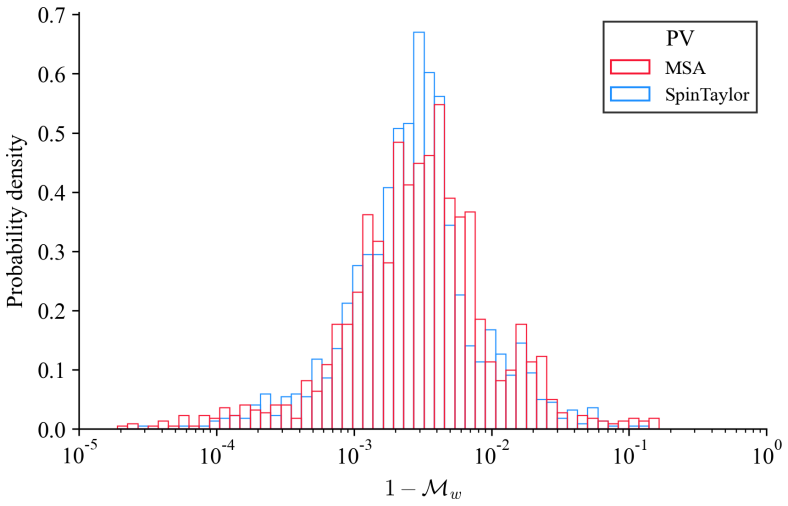

Figure 4: Histogram showing the probability density of the obtained SNR-weighted mismatch values when running the `MSA` and `SpinTaylor` precession versions of `IMRPhenomXP` against a set of SXS NR waveforms. The median and standard deviation are, respectively, 0.0031 and 0.0137 for `MSA`, together with 0.0028 and 0.0084 for `SpinTaylor`.

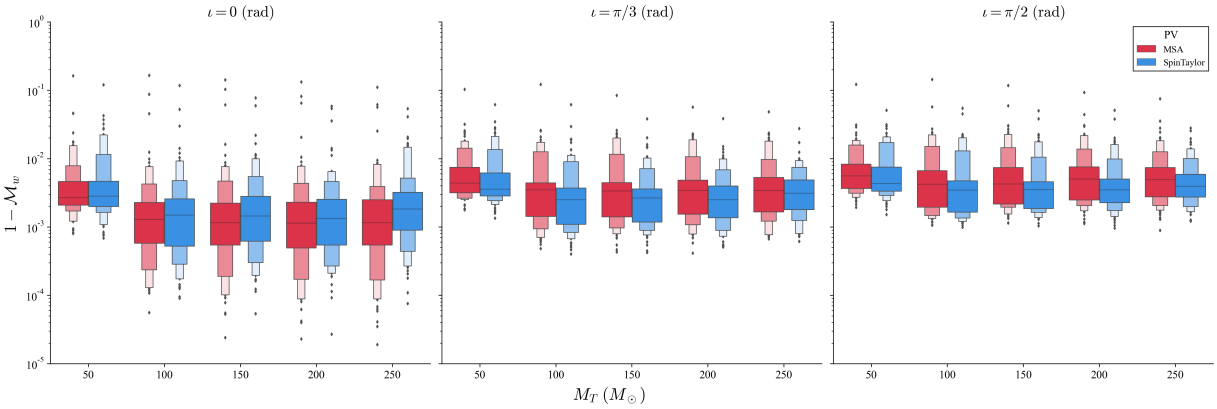

Figure 5: Box plots showing the SNR-weighted mismatch distribution of values obtained when running the `MSA` and `SpinTaylor` precession versions of `IMRPhenomXP` against a set of SXS NR waveforms. The results are broken down by inclination (ι) and total mass (M_T).

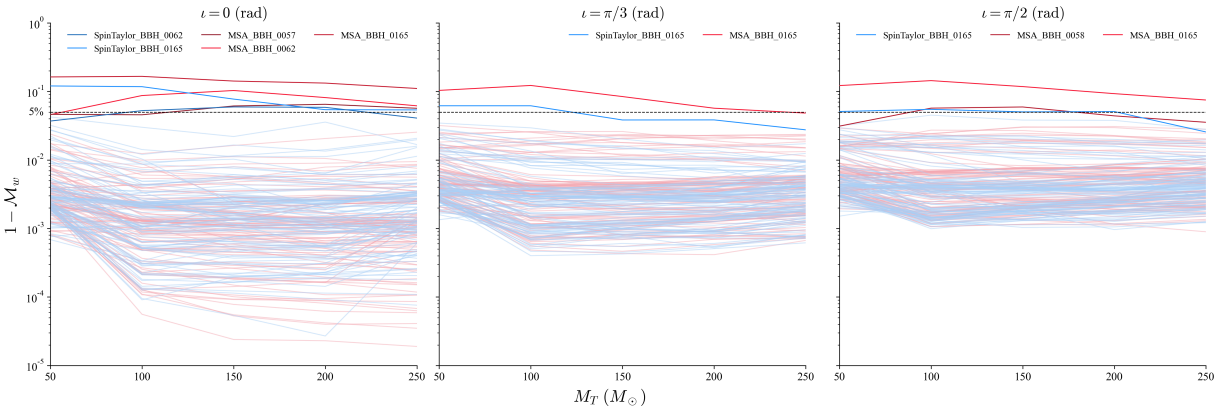

Figure 6: Line plots where each line shows the SNR-weighted mismatch values obtained when running the `MSA` and `SpinTaylor` precession versions of `IMRPhenomXP` against one of the employed SXS NR waveforms for a given inclination (ι) and each one of the selected total masses (M_T). The highlighted lines are those that have some point above the 5% mismatch.

magnitude above of what we found in the aligned-spin case. This extra discrepancy was to be expected due to the extra complexity added by precession, and, based on the results presented above, we estimate that the impact of a different aligned spin baseline is generally small. The precession differences can be isolated by matching the `SpinTaylor` and `MSA` precession versions of `IMRPhenomXP` against each other as in the third plot of fig. 9, where we do not observe as many mismatches as in the previous comparisons, but we do in any case observe a tail of mismatches above the 5% level. As can be seen in fig. 10, these mismatches have been found to correspond to inclination values close to 90° (where the effects of precession and higher modes are typically maximised) and polarization angles [20, 40] close to 45° which correspond to the lowest SNR's in the sample. Nonetheless, we do find a number of systems with SNR ≥ 15 showing matches below 95%, suggesting these effects might be distinguishable, though comparisons to NR simulations and injections studies would be needed to clarify this.

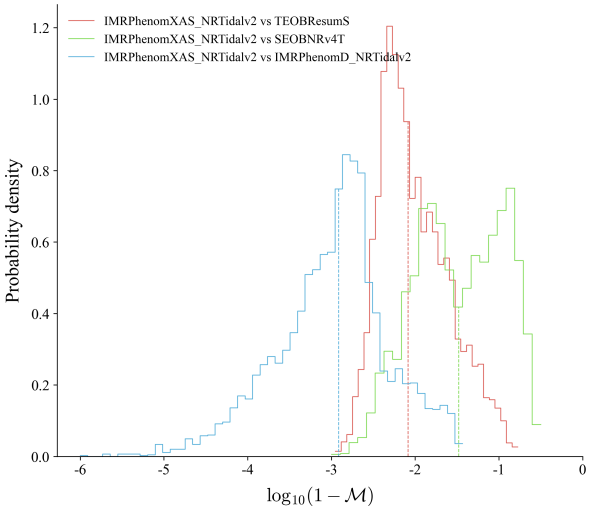

(a) `IMRPhenomXAS` with the `NRTidalv2` extension against `IMRPhenomD` with the same extension, `TEOBResumS` and `SEOBNRv4T`.

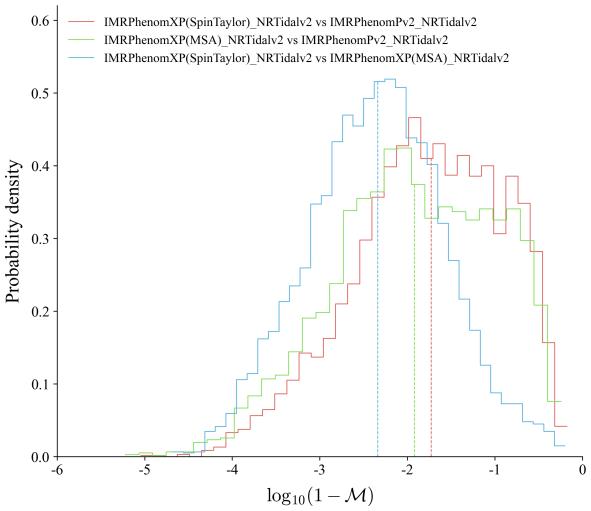

(b) `SpinTaylor` and `MSA` versions of `IMRPhenomXP` against `IMRPhenomPv2`, both with the `NRTidalv2` extension.

Figure 7: Histogram plots of logarithmic mismatch probability density for the aligned spin `IMRPhenomXAS` (a) and precessing `IMRPhenomXP` (b), both with the `NRTidalv2` extension, against a set of other tidal models. The dashed lines represent the median of their respective distribution.

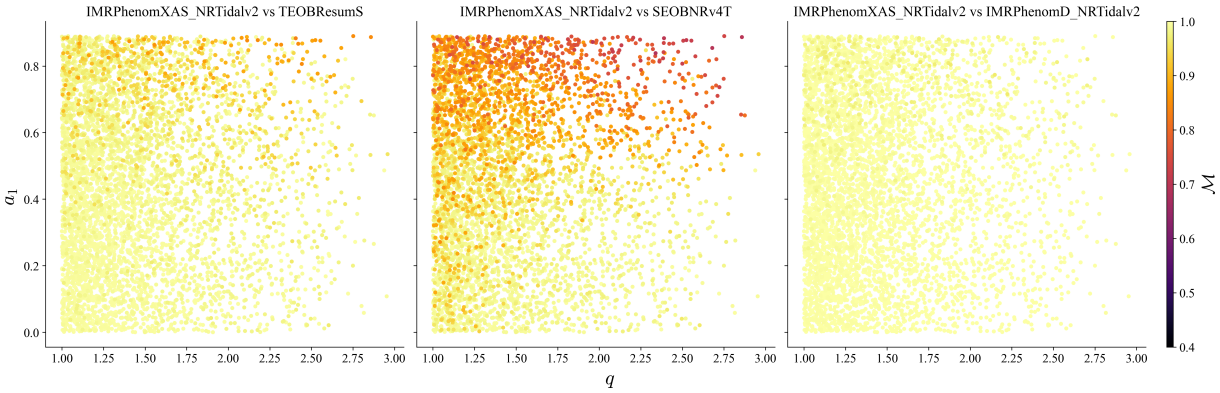

Figure 8: Scatter plot showing match values of `IMRPhenomXAS_NRTidalv2` against the same models and over the same random set of fig. 7a. The matches are sorted by mass ratio (q) and dimensionless spin of the most massive NS (a_1).

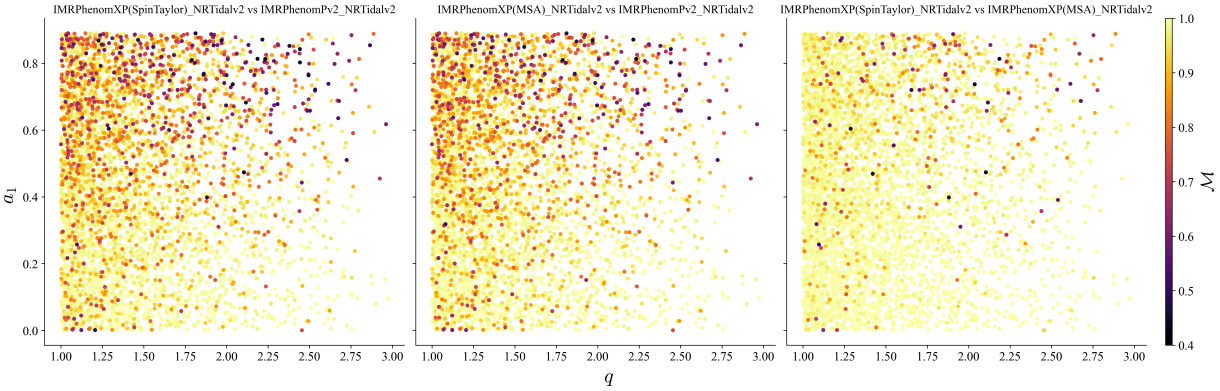

Figure 9: Scatter plot showing match values of `IMRPhenomXP_NRTidalv2` against the same models and over the same random set of fig. 7b. The matches are sorted by mass ratio (q) and dimensionless spin of the most massive NS (a_1).

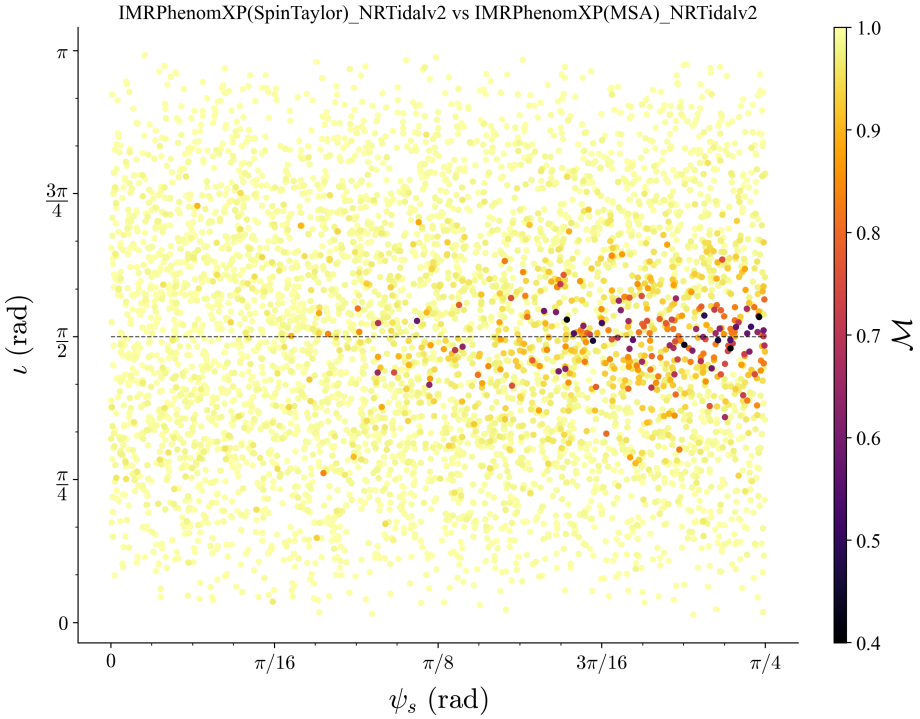

Figure 10: The same scatter plot presented in fig. 9 of the `SpinTaylor` and `MSA` precession versions of `IMRPhenomXP` against each other, but sorted by the polarization angle (ψ_s) and inclination (ι).

4.3 Timing Tests

We will now present timing tests for both `IMRPhenomXP_NRTidalv2` and the `SpinTaylor` version of `IMRPhenomXP`. Because the frequency domain is where noise is most easily characterized [21], and thus the domain of choice when performing parameter estimation, we will be presenting the waveforms' evaluation times in the frequency domain; meaning that time-domain models are at a disadvantage for their waveforms must be Fourier transformed, which increases the computational cost. The evaluations have been performed between 20 Hz and 2048 Hz with steps of $1/4$ Hz for the BBH baselines and of 0.0029 Hz for the tidal models. The frequency bins were adjusted to each system based on the duration of their GW signals with the help of the `lalapps_chirplen` function.

Starting with the precessing BBH baseline, it can be seen in fig. 11 how both options of the frequency-domain native `IMRPhenomXP` show better times than the time-domain `IMRPhenomTP`; especially with multibanding (MB) activated, where the analytical MSA approximation of the Euler angles is about one order of magnitude faster than the time-domain version. As expected, the numerical integration of the spin-precession equations (`SpinTaylor` in the plots) is a bit slower than the analytical MSA approximation, but still competitively fast.

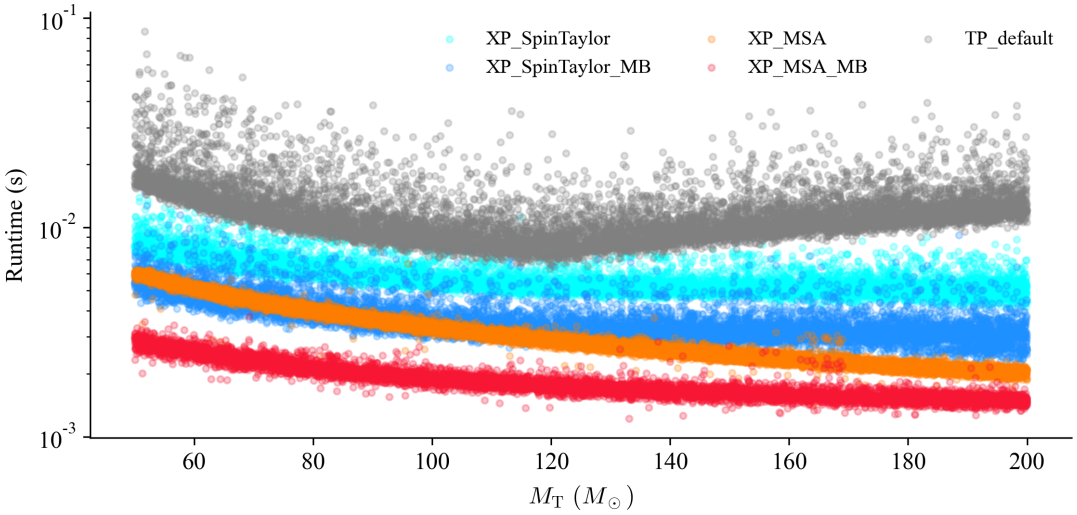

Figure 11: Runtimes of the `SpinTaylor` and `MSA` versions of `IMRPhenomXP` compared to the default version of `IMRPhenomTP` for the same random set of precessing BBH binaries, sorted by total mass. The `MB` on the version names stands for multibanding.

When higher modes are activated as in fig. 12, all running times become slower, but the same is observed: both frequency domain options are faster than the default time-domain version. Additionally, the numerical integration runtimes are now much closer to those of the analytical MSA approximation.

Regarding BNS systems, in the case of aligned spin, it can be seen in fig. 13 how the frequency-domain BBH baseline `IMRPhenomX` with the tidal extension `NRTidalv2`, is much faster than the numerical EOB `TEOBResumS` model, and almost a whole order of magnitude faster than the single-spin `IMRPhenomD` baseline with the same tidal extension. This is very relevant, for GWs coming from BNS systems are longer than those of BBH systems and thus much more expensive to analyze.

When precession is added into the mix as in fig. 14, `IMRPhenomXP` with the double-spin MSA analytical approximation is about twice as fast as the single-spin `IMRPhenomPv2` model. On the other hand, the more accurate numerical integration is about half as fast as `IMRPhenomPv2`.

As a final comment, inspirals present more cycles the lower the total mass, which translates into models being generally slower for lower masses, especially those that perform numerical evolution like `TEOBResumS` in fig. 13 and `XP_NRTidalv2_SpinTaylor` in fig. 14; which explains them showing the same behaviour.

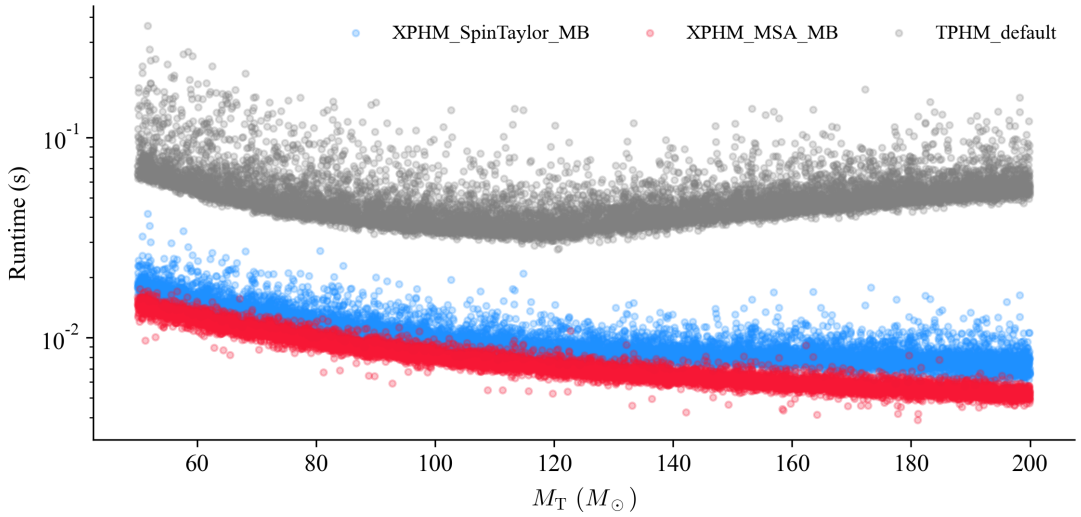

Figure 12: Runtimes of the `SpinTaylor` and `MSA` versions the high-modes frequency-domain model `IMRPhenomXPHM` compared to the default version of the high-modes time-domain model `IMRPhenomTPHM` over the same set of random precessing BBH systems.

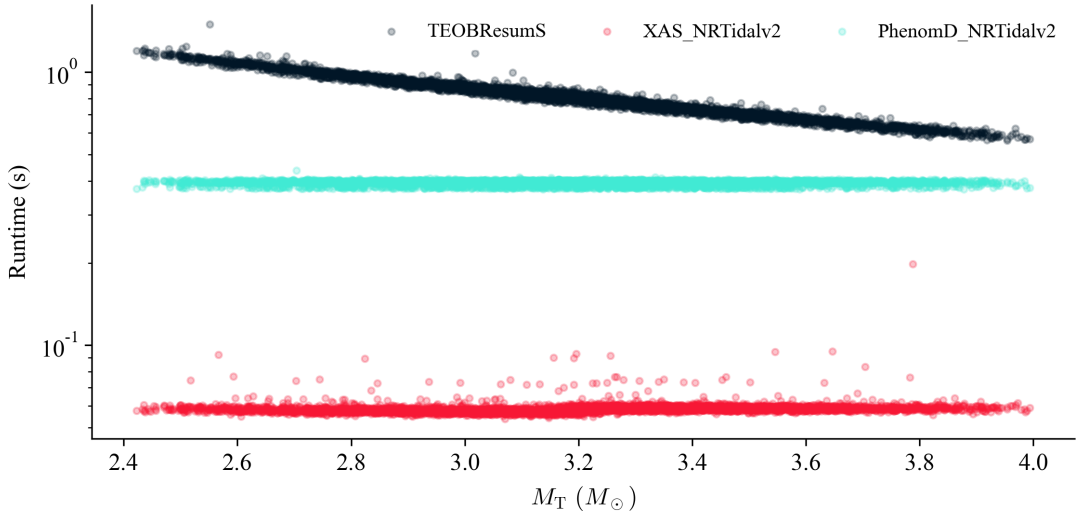

Figure 13: Runtimes of the `IMRPhenomX` BBH baseline with the `NRTidalv2` tidal extension compared to those of the `IMRPhenomD` baseline with the same tidal extension and those of the `TEOBResumS` tidal model over the same random set of aligned-spin BNS system.

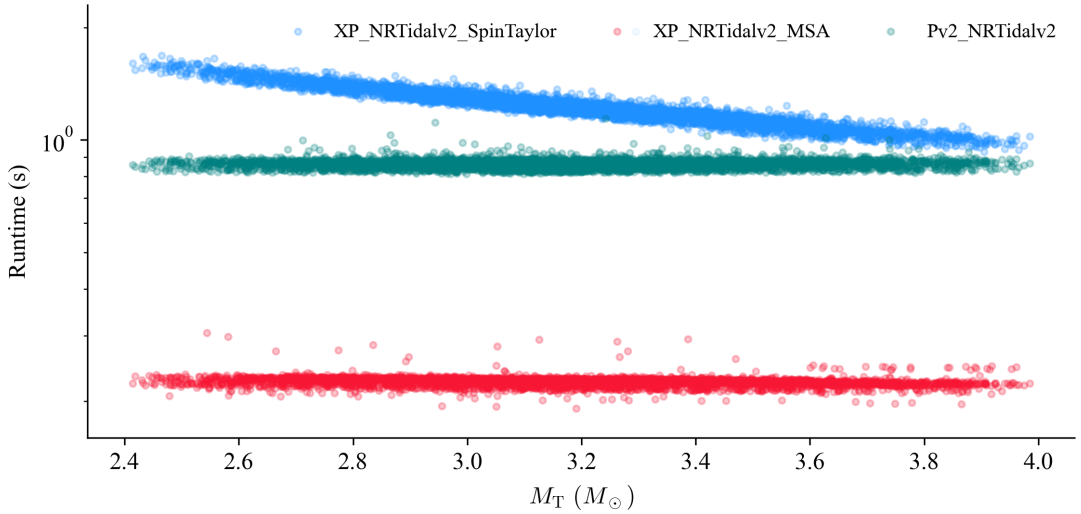

Figure 14: Runtimes of the numerical `SpinTaylor` and double-spin `MSA` analytical approximation of `IMRPhenomXP` compared to the single-spin `IMRPhenomPv2` model; all with the `NRTidalv2` extension over the same set of random precessing BNS systems.

5 Conclusion

In this thesis, we have presented the new frequency-domain phenomenological tidal model for BNS coalescences `IMRPhenomXP_NRTidalv2`. The model can be called with a new precession prescription where the spin-precession equations are numerically evolved, which was previously available only in time domain models. This provides extra opportunities to test how different treatments of precession impact the final template.

Our tests have shown that the new precession prescription produces matches against binary black-hole numerical relativity waveforms with less outliers than the current default, though at the expense of an increased computational cost.

Regarding the new tidal model, our tests have shown very good agreement with `IMRPhenomD_NRTidalv2`, `TEOBResumS` and `SEOBNRv4T` for aligned low-spin configurations, but growing differences for high-spin large mass-ratio configurations, especially with `SEOBNRv4T` (which currently offers a more complete description of tidal effects). It will be interesting to repeat this comparison with future versions of the `NRTidal` extension. For precessing configurations, the agreement within `Phenom` models is lost across all parameter space, especially when high spins are involved. Future comparisons against BNS precessing hybrids will help to assess the importance of double-spin effects for these systems, which are not modelled in `IMRPhenomPv2_NRTidalv2`. The two double-spin precession versions of `IMRPhenomXPHM` show less disagreement, though there is still a fraction of systems with good SNR showing matches below 95%, suggesting these effects might be distinguishable.

Regarding the waveform evaluation time of tidal models, we underline there is an order-of-magnitude improvement against `TEOBResumS` and `PhenomD_NRTidalv2` for aligned-spin BNS configurations; and, for precessing BNS configurations, the numerical integration has shown comparable times to those of the single-spin model `IMRPhenomPv2_NRTidalv2`, and half an order of magnitude improvement has been observed for the analytical `MSA` approximation.

References

[1] Geraint Pratten et al. "Computationally efficient models for the dominant and subdominant harmonic modes of precessing binary black holes". In: *Physical Review D* 103.10 (May 2021). DOI: 10.1103/physrevd.103.104056.

[2] Tim Dietrich et al. "Improving the NRTidal model for binary neutron star systems". In: *Physical Review D* 100.4 (Aug. 2019). DOI: 10.1103/physrevd.100.044003.

[3] The LIGO Scientific Collaboration. "LIGO: the Laser Interferometer Gravitational-Wave Observatory". In: *Reports on Progress in Physics* 72.7 (June 2009). DOI: 10.1088/0034-4885/72/7/076901.

[4] "GWTC-2: Compact Binary Coalescences Observed by LIGO and Virgo during the First Half of the Third Observing Run". In: *Physical Review X* 11.2 (June 2021). DOI: 10.1103/physrevx.11.021053.

[5] "GWTC-3: Compact Binary Coalescences Observed by LIGO and Virgo During the Second Part of the Third Observing Run". In: (Nov. 2021). DOI: 10.48550/ARXIV.2111.03606.

[6] Alexander H. Nitz et al. *4-OGC: Catalog of gravitational waves from compact-binary mergers*. Dec. 2021. DOI: 10.48550/ARXIV.2112.06878.

[7] Alicia M. Sintes José A. Font and Carlos F. Sopuerta. *Gravitational waves with the SKA*. 2015. DOI: 10.48550/ARXIV.1506.03474.

[8] David Tong. *General Relativity*. 2019. URL: http://www.damtp.cam.ac.uk/user/tong/gr/gr.pdf.

[9] M. Maggiore. *Gravitational Waves: Volume 1: Theory and Experiments*. Vol. 1. Gravitational Waves. OUP Oxford, 2008, pp. 337–339, 343–345. ISBN: 9780198570745.

[10] Chiara Caprini and Daniel G Figueroa. "Cosmological backgrounds of gravitational waves". In: *Classical and Quantum Gravity* 35.16 (July 2018), p. 163001. DOI: 10.1088/1361-6382/aac608.

[11] Éanna É Flanagan and Scott A Hughes. "The basics of gravitational wave theory". In: *New Journal of Physics* 7 (Sept. 2005), pp. 204–204. DOI: 10.1088/1367-2630/7/1/204.

[12] Eleanor Hamilton et al. "Model of gravitational waves from precessing black-hole binaries through merger and ringdown". In: *Physical Review D* 104.12 (Dec. 2021). DOI: 10.1103/physrevd.104.124027.

[13] Patricia Schmidt. "Gravitational Waves From Binary Black Hole Mergers: Modeling and Observations". In: *Frontiers in Astronomy and Space Sciences* 7 (2020). ISSN: 2296-987X. DOI: 10.3389/fspas.2020.00028.

[14] Lawrence E. Kidder. "Coalescing binary systems of compact objects to (post)$^{5/2}$ Newtonian order. V. Spin effects". In: *Physical Review D* 52.2 (July 1995), pp. 821–847. DOI: 10.1103/physrevd.52.821.

[15] B. P. Abbott et al. "Search for Eccentric Binary Black Hole Mergers with Advanced LIGO and Advanced Virgo during Their First and Second Observing Runs". In: *The Astrophysical Journal* 883.2 (Sept. 2019), p. 149. DOI: 10.3847/1538-4357/ab3c2d.

[16] Éanna É. Flanagan and Tanja Hinderer. "Constraining neutron-star tidal Love numbers with gravitational-wave detectors". In: *Physical Review D* 77.2 (Jan. 2008). DOI: 10.1103/physrevd.77.021502.

[17] Andreas Guerra Chaves and Tanja Hinderer. "Probing the equation of state of neutron star matter with gravitational waves from binary inspirals in light of GW170817: a brief review". In: *Journal of Physics G: Nuclear and Particle Physics* 46.12 (Nov. 2019), p. 123002. DOI: 10.1088/1361-6471/ab45be.

[18] Paolo Pani, Leonardo Gualtieri, and Valeria Ferrari. "Tidal Love numbers of a slowly spinning neutron star". In: *Physical Review D* 92.12 (Dec. 2015). DOI: 10.1103/physrevd.92.124003.

[19] Andrea Taracchini. "Inspiral-merger-ringdown models for spinning black-hole binaries at the interface between analytical and numerical relativity". PhD thesis. University of Maryland, 2014.

[20] Patricia Schmidt, Frank Ohme, and Mark Hannam. "Towards models of gravitational waveforms from generic binaries: II. Modelling precession effects with a single effective precession parameter". In: *Physical Review D* 91.2 (Jan. 2015). DOI: 10.1103/physrevd.91.024043.

[21] The LIGO and Virgo Scientific Collaborations. "A guide to LIGO–Virgo detector noise and extraction of transient gravitational-wave signals". In: *Classical and Quantum Gravity* 37.5 (Feb. 2020). DOI: 10.1088/1361-6382/ab685e.

[22] J.D.E. Creighton and W.G. Anderson. "Gravitational-Wave Physics and Astronomy: An Introduction to Theory, Experiment and Data Analysis". In: Wiley Series in Cosmology. Wiley, 2011. Chap. 7, pp. 269–347. ISBN: 9783527408863. DOI: https://doi.org/10.1002/9783527636037.ch7.

[23] Drew Garvin Keppel. "Signatures and Dynamics of Compact Binary Coalescences and a Search in LIGO's S5 Data". PhD thesis. California Institute of Technology, 2009. Chap. 5, pp. 46–50. DOI: 10.7907/03MS-2W96.

[24] Katerina Chatziioannou et al. "Constructing gravitational waves from generic spin-precessing compact binary inspirals". In: *Physical Review D* 95.10 (May 2017). DOI: 10.1103/physrevd.95.104004.

[25] Héctor Estellés et al. "New twists in compact binary waveform modeling: A fast time-domain model for precession". In: *Physical Review D* 105.8 (Apr. 2022). DOI: 10.1103/physrevd.105.084040. URL: https://doi.org/10.1103%2Fphysrevd.105.084040.

[26] Geraint Pratten et al. "Computationally efficient models for the dominant and subdominant harmonic modes of precessing binary black holes". In: *Physical Review D* 103.10 (May 2021). DOI: 10.1103/physrevd.103.104056.

[27] Alejandro Bohé et al. "Next-to-next-to-leading order spin–orbit effects in the near-zone metric and precession equations of compact binaries". In: *Classical and Quantum Gravity* 30.7 (Mar. 2013), p. 075017. DOI: 10.1088/0264-9381/30/7/075017.

[28] Serguei Ossokine et al. "Comparing post-Newtonian and numerical relativity precession dynamics". In: *Physical Review D* 92.10 (Nov. 2015). DOI: 10.1103/physrevd.92.104028.

[29] Cecilio García-Quirós et al. "Accelerating the evaluation of inspiral–merger–ringdown waveforms with adapted grids". In: *Classical and Quantum Gravity* 38.1 (Nov. 2020), p. 015006. DOI: 10.1088/1361-6382/abc36e.

[30] Tim Dietrich, Tanja Hinderer, and Anuradha Samajdar. "Interpreting binary neutron star mergers: describing the binary neutron star dynamics, modelling gravitational waveforms,

and analyzing detections". In: *General Relativity and Gravitation* 53.3 (Mar. 2021). DOI: 10.1007/s10714-020-02751-6.

[31] M. Maggiore. *Gravitational Waves: Volume 2: Astrophysics and Cosmology*. OUP Oxford, 2018. ISBN: 9780191074479.

[32] Eric Poisson and Clifford M. Will. *Gravity: Newtonian, Post-Newtonian, Relativistic*. Cambridge University Press, 2014. DOI: 10.1017/CBO9781139507486.

[33] Matteo Breschi et al. "Kilohertz gravitational waves from binary neutron star remnants: Time-domain model and constraints on extreme matter". In: *Physical Review D* 100.10 (Nov. 2019). DOI: 10.1103/physrevd.100.104029.

[34] Marcella Wijngaarden et al. "Probing neutron stars with the full premerger and postmerger gravitational wave signal from binary coalescences". In: *Physical Review D* 105.10 (May 2022). DOI: 10.1103/physrevd.105.104019.

[35] D J A McKechan, C Robinson, and B S Sathyaprakash. "A tapering window for time-domain templates and simulated signals in the detection of gravitational waves from coalescing compact binaries". In: *Classical and Quantum Gravity* 27.8 (Apr. 2010), p. 084020. DOI: 10.1088/0264-9381/27/8/084020.

[36] Lisa Barsotti et al. *The updated Advanced LIGO design curve*. Apr. 2018. URL: https://dcc.ligo.org/public/0149/T1800044/005/T1800044-v5.pdf.

[37] Michael Boyle et al. "The SXS collaboration catalog of binary black hole simulations". In: *Classical and Quantum Gravity* 36.19 (Sept. 2019), p. 195006. DOI: 10.1088/1361-6382/ab34e2.

[38] Alessandro Nagar et al. "Time-domain effective-one-body gravitational waveforms for coalescing compact binaries with nonprecessing spins, tides, and self-spin effects". In: *Physical Review D* 98.10 (Nov. 2018). DOI: 10.1103/physrevd.98.104052.

[39] Benjamin D. Lackey et al. "Surrogate model for an aligned-spin effective-one-body waveform model of binary neutron star inspirals using Gaussian process regression". In: *Physical Review D* 100.2 (July 2019). DOI: 10.1103/physrevd.100.024002.

[40] Maximiliano Isi. *Parametrizing gravitational-wave polarizations*. 2022. DOI: 10.48550/ARXIV.2208.03372.